

## PAPER

[View Article Online](#)  
[View Journal](#) | [View Issue](#)Cite this: *J. Mater. Chem. A*, 2021, 9, 25585

## Formulation of Li-metal-halide (LMX) solid state electrolytes through extensive first principles modelling†

Yuran Yu, <sup>ab</sup> Zhuo Wang <sup>\*ab</sup> and Guosheng Shao <sup>\*ab</sup>

Lithium-metal-halides (LMX) are getting more and more attractive as a potential class of solid-state electrolytes (SSEs) to enable high-performance all solid-state batteries (ASSBs), owing to their high oxidation potentials, good ductility, and reasonable resilience to humidity. However, reported LMX materials use high-cost metals with limited resources. Here in this work, we have carried out extensive first principles modelling to identify potential compounds by screening a wide range of LMX systems involving green and low-cost metals with large resources. This leads to the identification of several highly attractive candidates based on  $\text{LiMX}_3$ ,  $\text{Li}_2\text{MX}_4$ ,  $\text{Li}_3\text{MX}_6$  and  $\text{Li}_6\text{MX}_8$ , which are suitable to enable high energy density solid batteries using high-voltage cathodes.

Received 11th July 2021  
Accepted 28th October 2021

DOI: 10.1039/d1ta05849e

[rsc.li/materials-a](https://rsc.li/materials-a)

## Introduction

All solid-state lithium-ion batteries (ASSLBs) are regarded as potentially safe next-generation batteries with high energy densities.<sup>1,2</sup> To date, the most exploited SSEs have been based on either oxides or sulphides. While oxide SSEs are renowned for excellent stability against humid air<sup>3</sup> with wide electrochemical windows,<sup>4</sup> they are notorious for serious drawbacks such as very low  $\text{Li}^+$  conductivity (up to only about  $0.1 \text{ mS cm}^{-1}$ ) at room temperature (RT),<sup>5</sup> poor deformability,<sup>6</sup> and high synthesis temperatures above  $1000^\circ\text{C}$ .<sup>7</sup> On the other hand, sulfide SSEs are advantageous in terms of outstanding ionic conductivity rivaling that of current organic liquid electrolytes,<sup>8,9</sup> good plasticity even around room temperature,<sup>10</sup> and low synthesis temperature below  $500^\circ\text{C}$ .<sup>10</sup> The main weakness of the latter lies in their low oxidation potentials around only 2 V,<sup>11</sup> making them electrochemically incompatible with high-voltage cathode materials.<sup>12</sup>

Recently, halide SSEs based on  $\text{Li}_3\text{MX}_6$  ( $\text{M}^{3+}$ : trivalent metal ions; X: Cl/Br), such as  $\text{Li}_3\text{InCl}_6$ ,<sup>13,14</sup>  $\text{Li}_3\text{YCl}_6$ ,<sup>15,16</sup>  $\text{Li}_3\text{YBr}_6$ ,<sup>17</sup>  $\text{Li}_3\text{-ScCl}_6$  (ref. 18 and 19) and off-stoichiometry compositions of  $\text{Li}_{3-x}\text{M}_{1-x}\text{Zr}_x\text{Cl}_6$  ( $\text{M} = \text{Y, Er}$ ),<sup>20</sup> have attracted great attention owing to their high oxidation potentials to accommodate high-voltage cathodes such as  $\text{LiCoO}_2$  and NMC811. Their main shortcoming lies in the marginal RT ion conductivity with

activation energy higher than 0.3 eV, which is inadequate for practical solid batteries.<sup>21</sup> They are also based on expensive metals with very limited resources, with yttrium, rare-earth, scandium and indium being considered as depleting metal resources.<sup>22</sup>

Structurally, the hexagonal  $\text{Li}_3\text{MX}_6$  phase is made of the octahedral  $\text{MX}_6$  and  $\text{LiX}_6$  units (with  $\text{M}^{3+}$  or  $\text{Li}^+$  at the centre and  $\text{X}^-$  at corners). The  $\text{MX}_6$  units play an important role in maintaining the structural framework, so that structural integrity could be maintained when a  $\text{Li}^+$  hops into a neighbouring centre-vacant cage.<sup>23</sup> The close packing of cation-centred octahedrons could be the major reason limiting the transportation of  $\text{Li}^+$  ions out of the cages, so that the presence of vacancies on Li and/or M sites would then be necessary to assist long-range migration of the alkali ions.<sup>15,16</sup> Also, the hexagonal structure would only provide a one-dimensional channel along the *c*-axis, which is not ideal for a superb ionic conductor.<sup>16,24</sup> It would therefore be highly beneficial to formulate alternative LMX systems based on cheap materials with more sustainable and environmentally friendly metal resources, while maintaining the benefits of high ionic conductivity, wide electrochemical window and suitable mechanical properties.

In this work, we have carried out extensive first principles simulation, towards identifying such sustainable and green LMX candidates. Initial screening was performed using an octahedral factor derived from available data sources such as the Material Project webpage (weblink <https://www.materialsproject.org>) and handbooks on phase structures and phase diagrams. Intense first principles modelling in the framework of the density functional theory (DFT) was then followed to cover materials stability, electrochemical potential, ionic conductivity, and electrochemical performance. A series of novel LMX compounds are thus discovered, with

<sup>a</sup>State Center for International Cooperation on Designer Low-carbon & Environmental Materials (CDLCEM), Zhengzhou University, 100 Kexue Avenue, Zhengzhou, 450001, China. E-mail: gsshao@zzu.edu.cn; wangzh@zzu.edu.cn

<sup>b</sup>Zhengzhou Materials Genome Institute (ZMGI), Zhongyuanzhigu, Building 2, Xingyang, 450100, China

† Electronic supplementary information (ESI) available. See DOI: 10.1039/d1ta05849e

This journal is © The Royal Society of Chemistry 2021

The dynamic stability is assessed by the phonon band structure calculation using the supercell method with the frozen-phonon approximation.<sup>41,42</sup> This also provides entropy data to formulate free energies for the calculation of phase diagrams.

The energy of formation,  $E_f$ , for each  $\text{Li}_a\text{MX}_b$  compound is defined with respect to the total energies of the stable constituent phases,

$$E_f = (E_{\text{Li}_a\text{MX}_b} - E_{\text{MX}(b-a)} - aE_{\text{LiX}})/(a + b + 1) \quad (1)$$

$E_f$  defined against the stable constituent phases is termed as the energy above the hull. As a rule of thumb, metastable phases with energy above the hull below or very close to 0.025 eV per atom are highly likely to be synthesized experimentally owing to thermal fluctuation close to room temperature.<sup>43–45</sup>

Phases identified through the above process will then be subjected to assessment of key functional properties for solid electrolytes:

### Li<sup>+</sup> ion conductivity

This involves *ab initio* molecular dynamics (AIMD)<sup>46–50</sup> to assess the diffusion coefficient ( $D$ ) and associated ionic conductivity at elevated temperatures to safeguard tractable simulation to reach steady states. Each AIMD lasts for 180 ps after a pre-equilibrium run of 10 ps, and a time step of 2 fs in the NVT ensembles together with a Nosé–Hoover thermostat is employed.

### Electrochemical potential

The potential profile can be calculated using the VASP total energy of a series of low-energy intercalation/de-intercalation configurations. The average electrochemical potential  $V_{\text{AB}}$ , for the transition between state A ( $\text{Li}_x\Pi$ ) and state B ( $\text{Li}_{x+\Delta x}\Pi$ ), with reference to electrochemical potential *vs.*  $\text{Li}/\text{Li}^+$  is:<sup>26,48,51</sup>

$$\bar{V}_{\text{AB}} = -1/z \{ [E_{\text{total}}(\text{Li}_{x+\Delta x}\Pi) - E_{\text{total}}(\text{Li}_x\Pi)]/\Delta x - E_{\text{total}}(\text{Li}) \}, (2)$$

where  $x$  is the number of Li in the formula unit of  $\text{Li}_x\Pi$ , charge value  $z = 1$  for  $\text{Li}^+$ ,  $\Delta x$  is the change in the number of Li atoms, and  $\Pi$  refers to the collection of other constituents. While the USPEX is a dependable energy minimizer for each composition, the Alloy-Theoretic Automated Toolkit (ATAT)<sup>52,53</sup> is particularly powerful in identifying the low-energy configurations during intercalation or de-intercalation.

### Mechanical properties

Mechanical properties including full elastic tensor can be calculated, with properties such as bulk ( $B$ ), shear ( $G$ ) and Young's ( $E$ ) moduli, Poisson's ratio ( $\nu$ ), *etc.*, readily derived. Of particular interest for solid electrolytes are the  $E$  and  $G/B$  ratio. Young's modulus  $E$  measures the material stiffness, so that a low  $E$  corresponds to better ductility owing to easier elastic deformation. The  $G/B$  ratio is a measure of brittleness of materials and a low  $G/B$  ratio corresponds to better ductility due to easier plastic deformation during processing. Overall, a low  $E$

indicates a softened lattice, and a low  $G/B$  ( $<0.5$ ) such as that achievable in sulphides is highly attractive for good plasticity even around room temperature, and a high  $G/B$  ratio typical to anti-perovskite ( $>0.7$ ) is behind poor boundary quality and potential “boundary resistance”.<sup>21</sup>

## Results and discussion

### Octahedral factor

Ba, Mg, Ca, Al, Zn, Ti, Cu, Co, Mn, Ni, and Fe, are considered to occupy the M sites in  $\text{Li}_a\text{MX}_b$  ( $X = \text{Cl}, \text{Br}$ ) based on  $\text{Li}_6\text{MX}_8$ ,  $\text{Li}_4\text{MX}_6$ ,  $\text{Li}_3\text{MX}_6$ ,  $\text{Li}_2\text{MX}_4$ ,  $\text{LiMX}_4$  and  $\text{LiMX}_3$ . The octahedral factors for  $\text{LiX}_6$  and  $\text{MX}_6$  are assessed to make sure they meet the empirical geometric request as potential building units for LMX phases. Starting from binary lithium halides, the octahedral factors for  $\text{LiX}$  ( $X = \text{Cl}, \text{Br}$ ) phases are within the range from 0.281 to 0.57, and they are constructed into cubic lattices with octahedral  $\text{LiX}_6$  units. Binary lithium halides with  $T_f$  outside of this range are not made of octahedrons anymore, *e.g.* with  $T_f = 1.01$  (the  $\text{BaF}_2$  (mp-1029) is built by  $\text{BF}_8$  cubic units. We find that such a stability range also applies to other octahedral  $\text{MX}_6$  units. Taking  $\text{AlBr}_3$  (mp-23288) as an example, the octahedron factor is only 0.273, and the stable structure of  $\text{AlBr}_3$  is made of  $\text{AlBr}_4$  tetrahedrons instead. For  $\text{FeBr}_3$  (mp-23232) with a  $T_f$  of 0.281, octahedral units of  $\text{FeBr}_6$  become the basic building units for the stable structure. The calculated octahedral factors are summarized in Fig. 3, using ionic radii listed in Table S2.† Overall, we find more than 88 binary halide units that can satisfy such an octahedral factor range.

### Global energy minimization

Minimal energy structures for initially identified LMX systems that met the octahedral factor request are summarized in Fig. 4, and are identified from the USPEX global energy minimization or taken from the Materials Project database. When the symmetries of the compound from USPEX or Materials Project are different, the structure with a lower free energy will be selected for further consideration.

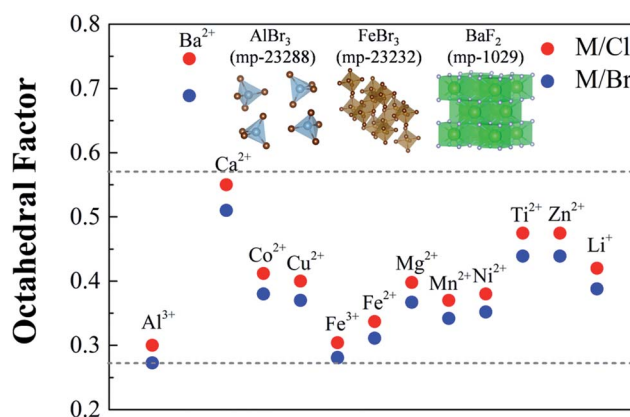


Fig. 3 Octahedral factors in the range 0.281–0.57 as possible M candidates.



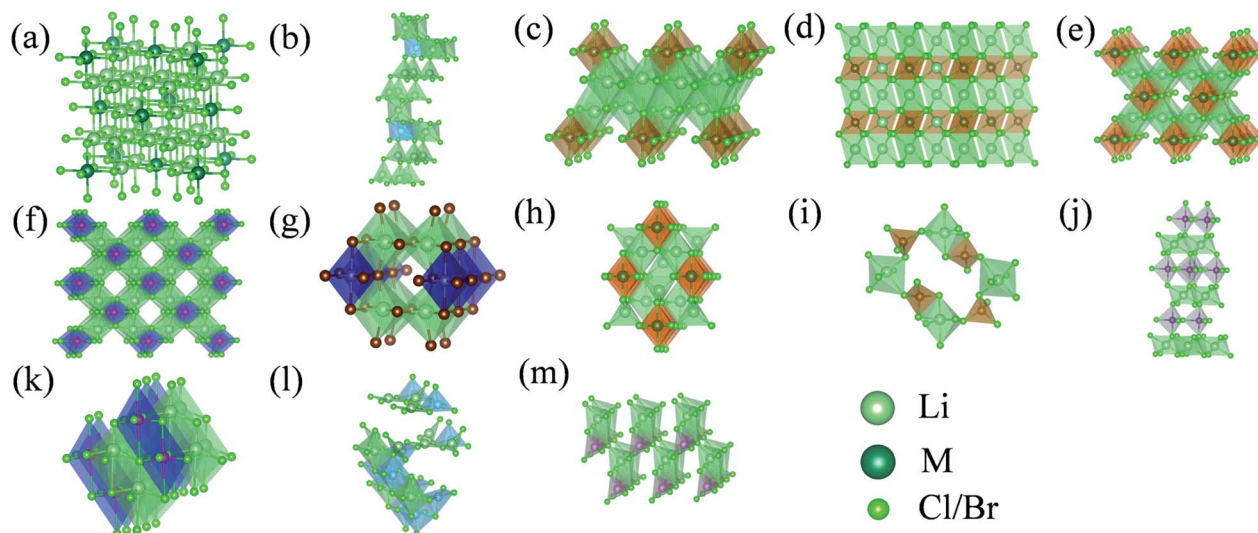


Fig. 4 Configurations of (a)  $\text{Li}_6\text{MX}_8$  ( $\text{M} = \text{Co}, \text{Cu}, \text{Fe}, \text{Mg}, \text{Mn}$ ),  $\text{Li}_6\text{NiCl}_8$ ; (b)  $\text{Li}_6\text{TiX}_8$ ; (c)  $\text{Li}_4\text{MX}_6$  ( $\text{M} = \text{Fe}, \text{Mn}, \text{Ti}$ ); (d)  $\text{Li}_3\text{AlCl}_6$ ,  $\text{Li}_3\text{FeX}_6$ ; (e)  $\text{Li}_2\text{TiX}_4$ ,  $\text{Li}_2\text{MnBr}_4$ ,  $\text{Li}_2\text{CoCl}_4$ ,  $\text{Li}_2\text{MgBr}_4$ ; (f)  $\text{Li}_2\text{CuX}_4$ ; (g)  $\text{Li}_2\text{CoBr}_4$ ; (h)  $\text{Li}_2\text{MgCl}_4$ ,  $\text{Li}_2\text{MnCl}_4$ ,  $\text{Li}_2\text{FeX}_4$ ; (i)  $\text{LiFeX}_4$ ; (j)  $\text{LiNiX}_3$ ; (k)  $\text{LiCuX}_3$ ; (l)  $\text{LiTiCl}_3$ ; (m)  $\text{LiZnCl}_3$ , which are identified from USPEX global energy minimization or from the Materials Project database.

For the composition of  $\text{Li}_6\text{MX}_8$  ( $\text{M} = \text{Co}, \text{Cu}, \text{Fe}, \text{Mg}, \text{Mn}, \text{Ni}$ ), the most stable structure obtained from USPEX is shown in Fig. 4(a), which is of a face-centred cubic lattice,  $\text{FM}\bar{3}\text{M}(225)$ .<sup>54–56</sup> Such a Suzuki structure is a rock salt derivative with an orderly arrangement of cation-centred ( $\text{Li}^+$  and  $\text{M}^{2+}$ ) octahedrons, which is also regarded as a deficient  $\text{LiCl}$ -type structure with “missing” octahedrons due to the presence of non-alkali cations assuming the nominal  $\text{M}^{2+}$  valency states.<sup>54–56</sup> On the other hand, the most stable configuration for the  $\text{Li}_6\text{TiX}_8$ , Fig. 4(b), has a rather different structure, where partial  $\text{Li}^+$  ions are confined in tetrahedrons resulting in a low-symmetry configuration of the  $\text{CM}$  space group (space group number 8).

The  $\text{Li}_4\text{MX}_6$  ( $\text{M} = \text{Fe}, \text{Mn}, \text{Ti}$ ) stoichiometry, Fig. 4(c), adopts the typical rock salt structure, stacked by cation ( $\text{Li}^+$  and  $\text{M}^{2+}$ ) centred octahedrons with a symmetry of  $\text{C2}/\text{M}(12)$ . The  $\text{Li}_4\text{MX}_6$  phase is constructed by alternately stacking two  $\text{Li}-\text{Cl}$  layers and one  $\text{M}-\text{Cl}$  layer.

For the composition of  $\text{Li}_3\text{MX}_6$  ( $\text{Li}_3\text{AlCl}_6$ ,  $\text{Li}_3\text{FeX}_6$ ), the valence state of  $\text{M}$  ( $\text{Al}, \text{Fe}$ ) is +3, which is also constructed by the  $\text{LiX}_6$  and  $\text{MX}_6$  octahedrons with the trigonal symmetry of  $\text{P}\bar{3}1\text{M}(162)$ , Fig. 4(d). Such a trigonal structure is similar to the experimentally synthesized  $\text{Li}_3\text{YCl}_6$  phase,<sup>15,16</sup> with neighbouring octahedrons sharing one common facet plane. It is very different from the aforementioned  $\text{Li}_6\text{MX}_8$  or  $\text{Li}_4\text{MX}_6$  phases, in which the neighbouring octahedrons only share a common edge.

Each of the  $\text{Li}_2\text{MX}_4$  ( $\text{Li}_2\text{MnBr}_4$ ,  $\text{Li}_2\text{TiX}_4$ ,  $\text{Li}_2\text{CoCl}_4$ ,  $\text{Li}_2\text{MgBr}_4$ ) phases, (Fig. 4(e)), possesses a spinel like structure with all  $\text{Li}^+$  ions located at the octahedral sites, resulting in a symmetry of  $\text{CMMM}(65)$ .<sup>57–59</sup> On the other hand,  $\text{Li}_2\text{CuX}_4$ , Fig. 4(f), has a lowered symmetry of  $\text{CM}(8)$  due to slight lattice distortion. The  $\text{Li}_2\text{CoBr}_4$  (Fig. 4(g)) is structurally similar to the spinel structure with a different symmetry of  $\text{PMMM}(47)$ . The  $\text{Li}_2\text{MgCl}_4$ ,  $\text{Li}_2\text{MnCl}_4$  and  $\text{Li}_2\text{FeX}_4$  (Fig. 4(h)) exhibit an inverse spinel

structure,  $\text{IMMA}(74)$ , with half of the  $\text{Li}^+$  ions located in tetrahedrons, and the other half of the  $\text{Li}^+$  cations located in octahedrons.<sup>60–62</sup>

For the composition of  $\text{LiMX}_4$ , the resultant  $\text{LiFeX}_4$  (Fig. 4(i)) is constructed with  $\text{FeX}_4$  tetrahedrons and  $\text{LiX}_6$  octahedrons alternately through their sharing an apex  $\text{X}$  anion to form the symmetry of  $\text{P2}_1/\text{C}(14)$ .

$\text{LiMX}_3$  ( $\text{M} = \text{M}^{2+}$ ;  $a = 1$ ,  $b = 3$ ) and  $\text{LiNiX}_3$  (Fig. 4(j)) have a trigonal symmetry of  $\text{R}\bar{3}\text{M}(160)$ , which is stacked by the  $\text{Li}^+$  centred octahedrons and  $\text{M}^{2+}$  centred hexahedrons. The rest of the compounds, such as  $\text{LiCuX}_3$  (Fig. 4(k)),  $\text{LiTiX}_3$  (Fig. 4(l)) and  $\text{LiZnCl}_3$  (Fig. 4(m)), exhibit highly distorted structures with lowered symmetry of  $\text{CM}(8)$ ,  $\text{CM}(8)$ , and  $\text{PM}(6)$ , correspondingly.

Further structural information for identified stable structures is summarized in Table S3.†

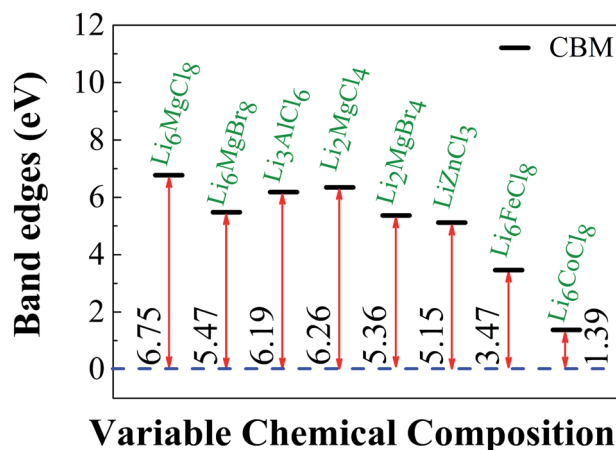


Fig. 5 The band gaps calculated using the HSE06 functional for identified compounds, with the zero Kelvin Fermi level corresponding to the valence band maximum (VBM) at 0 eV. Bandgap values between the VBM and the conduction band minimum (CBM) are shown.

## Bandgap

As SSEs need to be conductive to alkali ions but insulating to electrons, we need to have band gaps not lower than 2.5 eV.<sup>44,51</sup> The overall charge neutrality needs to be maintained, so that the materials are of intrinsic nature when they are semiconductors or insulators.

Fig. 5 shows the band gaps for compounds of interest, and the density of states (DOS) is displayed in Fig. S1.† The only phase with a low energy gap is  $\text{Li}_6\text{CoCl}_8$ , with a band gap value of only 1.39 eV, too low for a solid electrolyte but could be very useful for photovoltaic cells or photo-catalysts. Therefore, based on the bandgap values, compounds such as  $\text{Li}_6\text{MgCl}_8$ ,  $\text{Li}_6\text{MgBr}_8$ ,  $\text{Li}_3\text{AlCl}_6$ ,  $\text{Li}_2\text{MgCl}_4$ ,  $\text{Li}_2\text{MgBr}_4$  and  $\text{LiZnCl}_3$  could potentially serve as SSEs.

## Dynamic stability

A phase is dynamically stable when no phonon bands are associated with imaginary frequencies, so that all elastic tensor elements are real and the structure can thus sustain without the innate tendency to collapse. Fig. 6 shows calculated phonon band structures for various supercells of (a)  $\text{Li}_6\text{MgCl}_8$  ( $2 \times 2 \times 2$ , 120 atoms), (b)  $\text{Li}_6\text{MgBr}_8$  ( $2 \times 2 \times 2$ , 120 atoms), (c)  $\text{Li}_3\text{AlCl}_6$  ( $2 \times 2 \times 2$ , 80 atoms), (d)  $\text{Li}_2\text{MgCl}_4$  ( $2 \times 2 \times 1$ , 112 atoms), (e)  $\text{Li}_2\text{MgBr}_4$  ( $2 \times 2 \times 3$ , 84 atoms), and (f)  $\text{LiZnCl}_3$  ( $2 \times 3 \times 2$ , 60

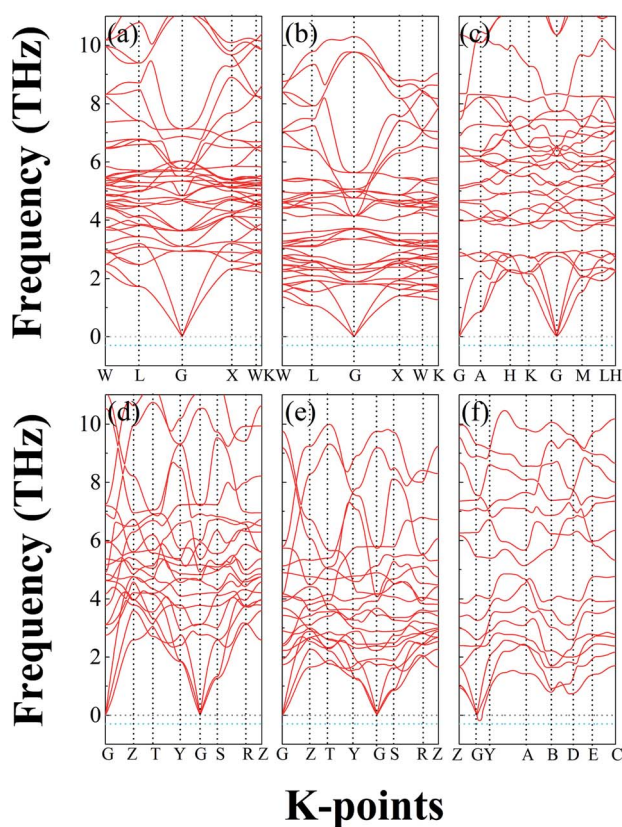


Fig. 6 Calculated phonon band structures for the minimal energy structures of (a)  $\text{Li}_6\text{MgCl}_8$ , (b)  $\text{Li}_6\text{MgBr}_8$ , (c)  $\text{Li}_3\text{AlCl}_6$ , (d)  $\text{Li}_2\text{MgCl}_4$ , (e)  $\text{Li}_2\text{MgBr}_4$ , and (f)  $\text{LiZnCl}_3$ .

atoms). The cyan lines represent the acceptable stability margin of  $-0.3$  THz in phonon calculations, which is out of consideration of the high sensitivity to remnant stress in the relaxed structures.<sup>41,42</sup> It can be seen from Fig. 6(a–e) that all identified phases of interest so far meet the dynamic stability criterion.

## Phase stability against stable constituents

Fig. 7 shows the equilibrium phase diagram for each compound of interest, with reference to the energies of stable binary phases, such as  $\text{MX}_2$  ( $\text{M} = \text{Mg}$  or  $\text{Zn}$ ;  $\text{X} = \text{Cl}$  or  $\text{Br}$ ) or  $\text{AlCl}_3$  and  $\text{LiX}$  ( $\text{X} = \text{Cl}$ , or  $\text{Br}$ ). The criterion for acceptable energy above the hull is set to be 0.025 eV per atom.<sup>43–45</sup> Starting from Fig. 7(a),  $\text{Li}_2\text{MgCl}_4$  is the only stable phase between the two binary constituents, with a formation energy of  $-0.00656$  eV per atom vs. that of the constituent  $\text{MgCl}_2$  and  $\text{LiCl}$  phases. The metastable phases are shown in open circles. Their formation energies are close to or lower than 0.025 eV per atom above the hull, and as was demonstrated in many well-established solid electrolytes such as the LGPS and argyrodites based sulphides, such phases could be fabricated at moderately elevated temperature and retained to serve under non-equilibrium conditions typically experienced in battery materials, Table S4.†

Similarly,  $\text{Li}_6\text{MgBr}_8$  (Fig. 7(b)),  $\text{LiAlCl}_4$  (Fig. 7(c)), and  $\text{Li}_2\text{ZnCl}_4$  as well as  $\text{Li}_4\text{ZnCl}_6$  (Fig. 7(d)) are stable phases on the convex bottom edge of the hull. Also,  $\text{Li}_2\text{MgBr}_4$ ,  $\text{Li}_4\text{MgBr}_6$ ,  $\text{LiZnCl}_3$ ,  $\text{Li}_6\text{ZnCl}_8$ , and  $\text{Li}_3\text{AlCl}_6$  are metastable phases highly likely to form due to the very small energy above the hull. Among such energetically favoured phases,  $\text{Li}_4\text{MgX}_6$ ,  $\text{Li}_2\text{ZnCl}_4$ ,  $\text{Li}_4\text{ZnCl}_6$ ,

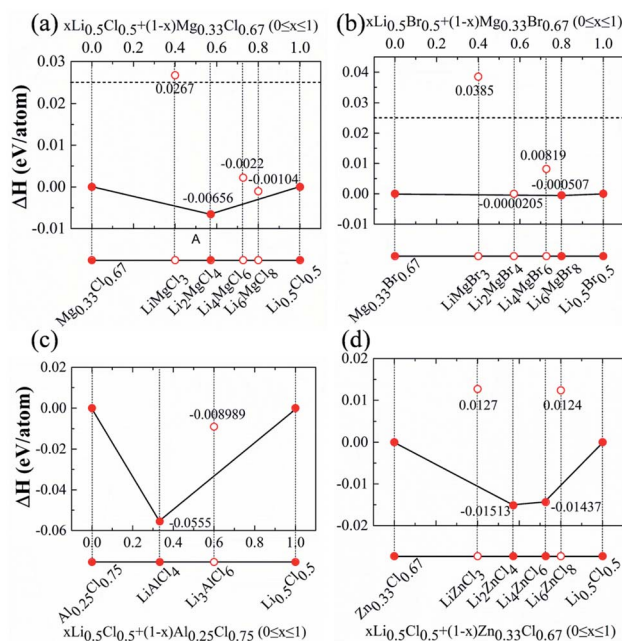


Fig. 7 Equilibrium phase diagram and formation energies for different alloys in the (a)  $\text{Li}_6\text{MgCl}_8$ , (b)  $\text{Li}_6\text{MgBr}_8$ , (c)  $\text{Li}_3\text{AlCl}_6$ , and (d)  $\text{Li}_2\text{ZnCl}_4$  systems, with reference to corresponding stable constituent phases. Filled circles are stable phases and metastable phases (open circles) with energy-above-the-hull below or very close to 0.025 eV are considered highly likely to be experimentally realized.

$\text{Li}_6\text{ZnCl}_8$ , and  $\text{LiAlCl}_4$  are structurally more compact with basic building blocks being tetrahedrons without the less compact octahedrons. Such more compact phases are not considered further, as they are not expected to enable favourable diffusion channels for lithium ions. Consequently, only  $\text{Li}_6\text{MgCl}_8$ ,  $\text{Li}_6\text{MgBr}_8$ ,  $\text{Li}_2\text{MgCl}_4$ ,  $\text{Li}_2\text{MgBr}_4$ ,  $\text{LiZnCl}_3$ , and  $\text{Li}_3\text{AlCl}_6$  will be considered further as potential electrolytes and the corresponding POSCARs are displayed in the ESI.

### Mechanical properties

The Pugh ratio ( $G/B$ ) is an indicator of plasticity of materials, which is reversely correlated with Poisson's ratio. Overall, typical sulphide electrolytes (e.g.,  $\text{Li}_6\text{PS}_5\text{Cl}$  and LGPS) are the most ductile with a low  $G/B$  ratio ( $<0.5$ ). For most oxides, the  $G/B$  ratios are between 0.5 and 0.6, while the high  $G/B$  ratio in antiperovskites (e.g.  $\text{Li}_3\text{OCl}$   $>0.7$ ) indicates innate brittleness.<sup>63</sup> It is noted that the  $G/B$  ratio of  $\text{Li}_2\text{MgCl}_4$  is the lowest and except for the most elastic  $\text{LiZnCl}_3$ , halides identified in this work have similar  $G/B$  ratios typical for good oxide SSEs such as LLZO.

Elastic properties are important for solid electrolytes.<sup>63</sup> Table 1 lists the mechanical properties for halide compounds of interest. A low Young's modulus  $E$  corresponds to weaker resistance to elastic strain and better elasticity. Typical sulphide SSEs, such as  $\text{Li}_6\text{PS}_5\text{Cl}$  and LGPS, have Young's moduli in the order of 20 GPa and beneficial elasticity, while oxide materials such as  $\text{Li}_7\text{La}_3\text{Zr}_2\text{O}_{12}$  (LLZO) have much higher  $E$  over 150 GPa, and are very stiff and strong but rather brittle due to poor elasticity.<sup>63</sup> As is recognized, softer SSEs tend to have better ionic conductivity.<sup>48,64,65</sup> As shown in Table 1,  $E$  values for the selected halide compounds are closer to those of the sulphide SSEs, with the  $E$  value for the  $\text{LiZnCl}_3$  being the lowest (16.431 GPa) indicating very soft and elastic nature.

### $\text{Li}^+$ transportation through AIMD

The diffusion coefficients ( $D$ ) of alkali ions in solid electrolytes can be readily quantified using *ab initio* molecular dynamics (AIMD), at elevated temperature to quicken convergence necessary for tractable DFT simulation. The ion conductivity is linked to the diffusion coefficient *via* the Earnest–Eisenstein relationship.<sup>46–48,51,66</sup>

**Table 1** Calculated mechanical properties, including bulk modulus ( $B$ ), shear modulus ( $G$ ), Young's modulus ( $E$ ), Poisson's ratio ( $\nu$ ), and  $G/B$  ratio

Formula	$B$ (GPa)	$G$ (GPa)	$E$ (GPa)	$\nu$	$G/B$
$\text{Li}_2\text{MgCl}_4$	28.938	13.067	34.046	0.304	0.45
$\text{Li}_2\text{MgBr}_4$	19.733	11.632	29.172	0.254	0.59
$\text{Li}_3\text{AlCl}_6$	17.862	9.918	25.018	0.267	0.555
$\text{Li}_6\text{MgCl}_8$	27.897	17.103	42.599	0.246	0.613
$\text{Li}_6\text{MgBr}_8$	22.565	13.59	33.951	0.249	0.602
$\text{LiZnCl}_3$	8.172	7.053	16.431	0.165	0.863
$\text{Li}_6\text{PS}_5\text{Cl}^{64}$	28.7	8.1	22.1	0.37	0.28
LGPS <sup>64</sup>	27.3	7.9	21.7	0.37	0.29
$\text{Li}_7\text{La}_3\text{Zr}_2\text{O}_{12}$ (ref. 64)	127.4	68.9	175.1	0.27	0.54
$\text{Li}_3\text{OCl}^{64}$	55.7	41.5	99.7	0.2	0.74

The resultant diffusion data are presented in Fig. 8, with logarithmic values of  $D$  versus the reverse of temperature  $1000/T^{-1}$ . The linear correlations demonstrate typical Arrhenius relationships, which result in activation energies and extrapolated data at lower temperature. While the AIMD needs to be carried out at elevated temperatures to safeguard tractable temporal evolution in the framework of DFT simulation, the extrapolated values to low temperatures have been shown to be quite dependable, as summarized in Fig. 2 of ref. 66, which demonstrates excellent agreement between experimental and predicted ionic conductivities in alloys based on an argyrodite sulfide system.

Data derived from Fig. 8 are summarized in Table 2. Among the selected SSEs,  $\text{LiZnCl}_3$  has the highest ionic conductivity of  $8.89 \text{ mS cm}^{-1}$  at room temperature, with the smallest activation energy (0.242 eV) matching that of the LGPS sulphides. The others ( $\text{Li}_2\text{MgCl}_4$ ,  $\text{Li}_2\text{MgBr}_4$ ,  $\text{Li}_6\text{MgCl}_8$  and  $\text{Li}_6\text{MgBr}_8$ ) have moderate ionic conductivities evidently lower than the marker value of  $1 \text{ mS cm}^{-1}$  (300 K) for practical solid electrolytes, and their activation energy higher than 0.3 eV is also well above those of the best sulphides.<sup>8,48,51</sup> This is not shocking in that the best performer  $\text{LiZnCl}_3$  has the least compact structure, Fig. 2(m), and other phases such as the  $\text{Li}_6\text{MgX}_8$ ,  $\text{Li}_2\text{MgBr}_4$  and  $\text{Li}_3\text{AlCl}_6$  have close-packed octahedrons as shown in Fig. 2(a), (h) and (d) correspondingly. One notes that in close-packed  $\text{LiX}_6$  octahedrons, the lithium ions are imprisoned within halogen cages, and this makes their escaping rather difficult unless some vacancies are present in such compounds. As was found out experimentally, the presence of vacancies is really necessary in order to enhance lithium ion conductivity in hexagonal  $\text{Li}_3\text{MX}_6$  such as  $\text{Li}_3\text{InCl}_6$ ,<sup>13,14</sup>  $\text{Li}_3\text{YCl}_6$ ,<sup>15,16</sup>  $\text{Li}_3\text{YBr}_6$ ,<sup>17</sup> and  $\text{Li}_3\text{ScCl}_6$ .<sup>18,19</sup>

Let us find out how the presence of vacancies affects the ionic conductivity in these materials. Starting with the most compact structures of  $\text{Li}_6\text{MgX}_8$ , we introduce a pair of Li and Cl vacancies in the system of 60 atoms to maintain the overall charge neutrality. One can see from the data summarized in

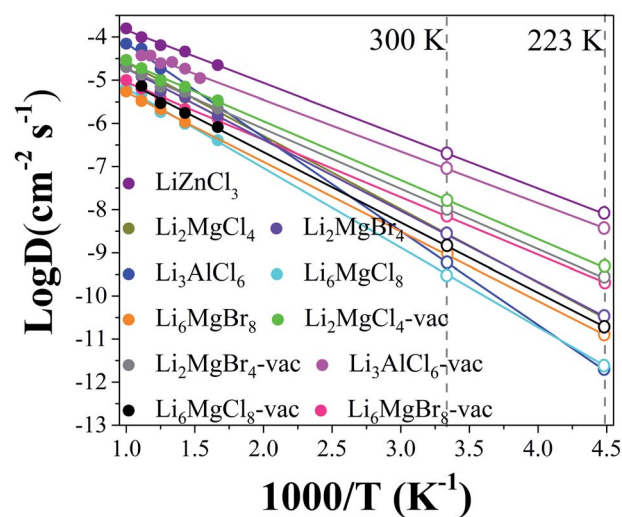


**Fig. 8** Diffusion coefficients for lithium ions obtained from AIMD simulation. The  $D$  values at 300 K and 223 K are presented as open circles.



Table 2 Summary of lithium ion transportation data from this work

System	Activation barrier (eV)	$D_0$ (cm <sup>2</sup> s <sup>-1</sup> )	Density (10 <sup>-23</sup> cm <sup>-3</sup> )	$D_{300K}$ (cm <sup>2</sup> s <sup>-1</sup> )	$\sigma$ (mS cm <sup>-1</sup> )		Li-vac/atom <sup>a</sup>
					300 K	223 K	
LiZnCl <sub>3</sub>	0.242	$2.398 \times 10^{-3}$	25.81	$2.027 \times 10^{-7}$	8.98	0.165	
Li <sub>2</sub> MgCl <sub>4</sub>	0.337	$1.3 \times 10^{-3}$	20.72	$2.79 \times 10^{-9}$	0.24	$2.648 \times 10^{-3}$	
Li <sub>2</sub> MgBr <sub>4</sub>	0.327	$8.354 \times 10^{-4}$	24.386	$2.644 \times 10^{-9}$	0.193	$2.439 \times 10^{-3}$	
Li <sub>3</sub> AlCl <sub>6</sub>	0.43	0.0107	21.215	$6.02 \times 10^{-10}$	0.053	$1.665 \times 10^{-4}$	
Li <sub>6</sub> MgCl <sub>8</sub>	0.365	$4.487 \times 10^{-4}$	18.488	$3.02 \times 10^{-10}$	0.043	$3.263 \times 10^{-4}$	
Li <sub>6</sub> MgBr <sub>8</sub>	0.32	$2.165 \times 10^{-4}$	22.558	$9.04 \times 10^{-10}$	0.1	$1.4 \times 10^{-3}$	
Li <sub>2</sub> MgCl <sub>4</sub> -vac	0.27	$6.082 \times 10^{-4}$	21.1	$1.697 \times 10^{-8}$	1.414	0.0378	1/112
Li <sub>2</sub> MgBr <sub>4</sub> -vac	0.276	$4.627 \times 10^{-4}$	2498	$1.043 \times 10^{-8}$	0.73	0.0182	1/84
Li <sub>3</sub> AlCl <sub>6</sub> -vac	0.237	$8.694 \times 10^{-4}$	21.484	$9.863 \times 10^{-8}$	7.524	0.315	1/80
Li <sub>6</sub> MgCl <sub>8</sub> -vac	0.323	$3.95 \times 10^{-4}$	19.126	$1.448 \times 10^{-9}$	0.185	$1.4 \times 10^{-3}$	1/60
Li <sub>6</sub> MgBr <sub>8</sub> -vac	0.264	$1.924 \times 10^{-4}$	23.336	$7.022 \times 10^{-9}$	0.744	0.022	1/60

<sup>a</sup> Numbers of Li and X vacancies are the same to maintain the overall charge neutrality.

Table 2 that the ionic conductivity in the vacancy containing Li<sub>6</sub>MgX<sub>8</sub>-vac can be significantly improved. In particular, the room-temperature (RT) conductivity in Li<sub>6</sub>MgCl<sub>8</sub>-vac and Li<sub>6</sub>MgBr<sub>8</sub>-vac will increase to 0.185 mS cm<sup>-1</sup> and 0.744 mS cm<sup>-1</sup>, several times higher than those in perfect crystals of Li<sub>6</sub>MgCl<sub>8</sub> and Li<sub>6</sub>MgBr<sub>8</sub>, while the activation energies of Li<sub>6</sub>MgCl<sub>8</sub>-vac and Li<sub>6</sub>MgBr<sub>8</sub>-vac will be reduced by 11.5% and 17.3%, respectively. A similar vacancy effect holds in the case of spinel like Li<sub>2</sub>MgX<sub>4</sub> compounds, and the predicted ionic conductivity (Table 2) is comparable to the experimental finding in the case of Li<sub>2</sub>Sc<sub>2/3</sub>Cl<sub>4</sub>. Li<sub>2</sub>Sc<sub>2/3</sub>Cl<sub>4</sub> had the same crystalline structure and nearly the same lattice parameter as Li<sub>2</sub>MgCl<sub>4</sub> identified here but contained a third of vacancies on the metal sites due to the higher valency of Sc<sup>3+</sup>, thus leading to a fairly good Li<sup>+</sup> conductivity of 1.5 mS cm<sup>-1</sup> at room temperature.<sup>18</sup>

Overall, the Li<sup>+</sup> transportation mechanism in halides from close packing of cation-centred octahedrons is rather different from other octahedron containing compounds wherein the lithium cations are not confined within each octahedral cage. For example, superb ionic conductivity can be achieved in sulphides with anti-perovskites,<sup>67–69</sup> or argyrodites<sup>51</sup> phases, where the Li<sup>+</sup> ions form the octahedral cages instead. In the case of the current halides with close-packed LiX<sub>6</sub> as the dominant building units, the presence of vacancies is key to enhancing the effective hopping of lithium ions, with charge neutrality *via* balanced anion vacancies playing a synergistic role.

In terms of structural characteristics, the Li<sub>3</sub>AlCl<sub>6</sub> phase is made of alternating LiCl<sub>6</sub> and AlCl<sub>6</sub> octahedrons, Fig. 4(d). Being similar to the Li<sub>6</sub>MgX<sub>8</sub> phases, without the presence of vacancies, the ionic conductivity in such a less compact phase is not good either (Table 2). If we introduce a pair of Li and Cl vacancies into the system of 80 atoms, radical improvement of the ionic conductivity is achieved, so that the RT conductivity of lithium ions increases over 100 times from 0.05 to 7.524 mS cm<sup>-1</sup> and the activation energy reduces 45% from 0.43 to 0.237 eV. Such ionic conductivity is close to that in the LiZnCl<sub>3</sub> phase, which has an evidently less compact structure, Fig. 4(m). Examining the pair correlation functions (PCF) before and after AIMD evolution at elevated temperatures shows that structural

disordering occurs in both the Li<sub>3</sub>AlCl<sub>6</sub>-vac and the LiZnCl<sub>3</sub> phases (Fig. 9). Fig. 9(a–c) show PCF between Li–Cl, Al–Cl and Li–Al. It is seen in Fig. 9(a) that the major peak at about 0.26 nm is reduced due to AIMD at 650 and 900 K, leading to significant enhancement of the minor peak at about 0.225 nm. For the PCF of Al–Cl, one also notes shifting of the peak to lower pair spacings. Such reduction of pair spacing between anions and cations is evidence of the reduced range of chemical ordering, with the second nearest neighbourhood being reduced and the nearest neighbourhood being enhanced. On the other hand, PCF between Al and Li cations is rather poor after AIMD, Fig. 9(c), indicating the lack of chemical association between cations.<sup>70</sup> Overall, the statistically reduced anion–cation pair spacing in the Li<sub>3</sub>AlCl<sub>6</sub>-vac over AIMD evolution is indicative of the shortened range of chemical ordering, so that the material containing vacancies of both Li and Cl tends to promote a glass-like transition with radically enhanced ionic transportation. Checking the change of activation energies owing to the presence of Li and Cl vacancies, it is found that the activation energy in the vacancy containing material is about 55% of that in the perfect crystal. Such a level of reduction of activation energy for mass transportation is also about the average level between single crystalline and glassy materials.<sup>71</sup> As was demonstrated by Goodenough and co-workers, promotion of glass formation is highly helpful for significant enhancement of ionic conductivity in anti-perovskite based solid electrolytes.<sup>72</sup>

Such shortening of the chemical ordering range is also evidenced in the less compact LiZnCl<sub>3</sub> phase, Fig. 9(d–f), so that similar disordering is behind high ionic conductivity. It is understandable that a less compact material tends to make it easier for disordering and glass formation. The mean square displacements (MSD) for these two disordered systems are shown in Fig. S2,† which shows that long range diffusion is dictated by the hopping of Li<sup>+</sup> ions in both cases. The fact that other ions do not diffuse far is actually beneficial to the structural integrity of solid electrolytes, since long-range diffusion of species other than Li<sup>+</sup> could lead to unwanted structural transitions. In addition, the ln MSD data for Li<sub>3</sub>AlCl<sub>6</sub>-vac and LiZnCl<sub>3</sub> at 900 K are plotted against ln(*t*) to determine the Li<sup>+</sup>

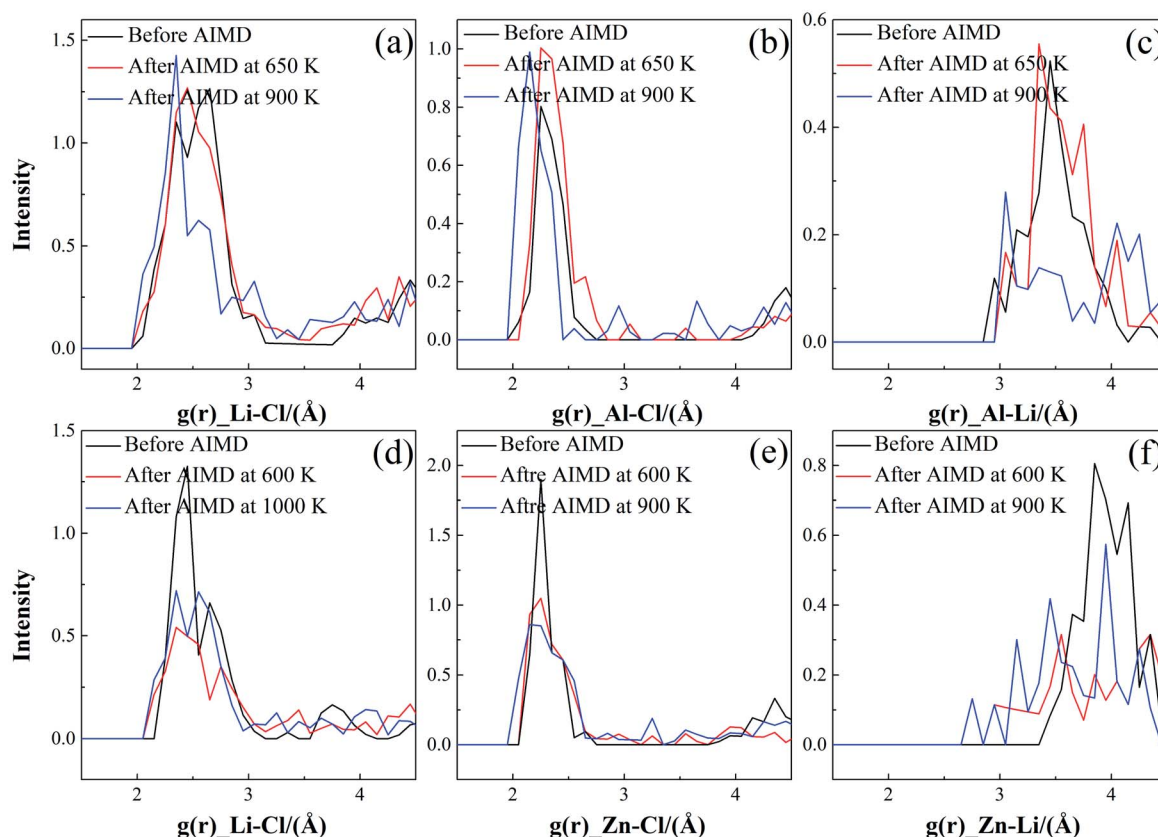


Fig. 9 Pair correlation functions (PCFs) for (a) Li–Cl, (b) Al–Cl, and (c) Al–Li bonds of  $\text{Li}_3\text{AlCl}_6$  after AIMD simulation at 650 K and 900 K; and PCFs for (d) Li–Cl, (e) Zn–Cl, and (f) Zn–Li bonds of  $\text{LiZnCl}_3$  after AIMD simulation at 600 K and 900 K.

diffusion coefficient  $D_{\text{Li}}$  and diffusion exponent  $\alpha_{\text{Li}}$ .<sup>73</sup> The calculated MSD as a function of  $t$  is fitted into the equation  $\text{MSD} = 2dD \times t^\alpha$ , which is linearized by logarithmic transformation to  $\ln \text{MSD} = \alpha \ln(t) + \ln(2dD)$ . The  $\alpha_{\text{Li}}$  values in both systems are close to 1, which represents the typical Arrhenius diffusion

relationship. The high  $D_{\text{Li}}$  values of about  $10^{-4} \text{ cm}^2 \text{ s}^{-1}$  are behind their excellent ionic transportation performance.

### Reduction and oxidation potential vs. Li

The oxidation potential is due to de-lithiation, and the reduction potential is attributed to lithiation, which can be readily assessed using the ATAT simulation to obtain total energy data and predict the associated chemical potentials according to eqn (2).<sup>26,74</sup> Thermodynamically, the negative directive of the total energy against the lithium content,  $\partial E_{\text{tot}}/\partial x$ , for each compound identified in this work suggests a natural tendency for lithiation. De-lithiation, on the other hand, leads to a quite high oxidation potential suitable for high voltage cathodes with open circuit voltage about and even well above 4 V, as shown in Fig. 10. In comparison, the oxidation potentials of typical sulphide-based solid electrolytes are much lower, e.g. LGPS (2.14 V) and  $\text{Li}_6\text{PS}_5\text{Cl}$  (2.01 V).<sup>11</sup>

## Conclusion

High-throughput DFT modelling has been carried out to identify potential halide SSEs based on sustainable and environmentally friendly material resources. A series of compounds have been found to be attractive solid electrolyte candidates, including  $\text{LiZnCl}_3$ ,  $\text{Li}_2\text{MgCl}_4$ ,  $\text{Li}_2\text{MgBr}_4$ ,  $\text{Li}_3\text{AlCl}_6$ ,  $\text{Li}_6\text{MgCl}_8$ , and

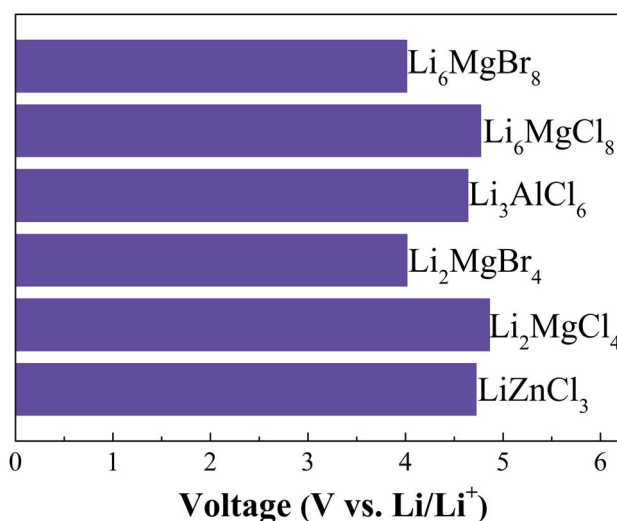


Fig. 10 Plot of Li uptake per formula unit of solid electrolyte against voltage vs.  $\text{Li/Li}^+$ .



$\text{Li}_6\text{MgBr}_8$ . All these phases are found to be very resilient to high voltage necessary for solid batteries of high energy densities.

Except for the  $\text{LiZnCl}_3$  phase, which is not constructed by close-packed polyhedrons, the presence of vacancies is found to be necessary to enable high ion conductivity with low activation energy. This is attributed to the confinement of  $\text{Li}^+$  within octahedron cages of halogen anions, so that vacancies play an essential role in opening escaping channels for the imprisoned alkali ions.

The best ionic conductors from this work are  $\text{LiZnCl}_3$  and the vacancy-containing  $\text{Li}_3\text{AlCl}_6$  compounds. They exhibit fast ionic transportation rivalling that of well-established sulphides such as LGPS or Li-argyrodites, and they are resilient to high cathode voltage above 4.5 V. The remarkable transportation characteristics are associated with a reduced range of chemical ordering over molecular dynamics evolution, which suggests the potential to use the materials in the amorphous form.

## Conflicts of interest

There are no conflicts to declare.

## Acknowledgements

This work is supported in part by the 1000 Talent Programme, the Zhengzhou Materials Genome Institute, the National Natural Science Foundation of China (No. 51001091, 111174256, 91233101, 51602094, and 11274100), and the Fundamental Research Program from the Ministry of Science and Technology of China (no. 2014CB931704).

## Notes and references

- 1 M. Tatsumisago, M. Nagao and A. Hayashi, *J. Asian Ceram. Soc.*, 2013, **1**, 17–25.
- 2 K. Takada, *Acta Mater.*, 2013, **61**, 759–770.
- 3 G. Liu, D. Xie, X. Wang, X. Yao, S. Chen, R. Xiao, H. Li and X. Xu, *Energy Storage Mater.*, 2019, **17**, 266–274.
- 4 X. Han, Y. Gong, K. Fu, X. He, G. T. Hitz, J. Dai, A. Pearse, B. Liu, H. Wang, G. Rubloff, Y. Mo, V. Thangadurai, E. D. Wachsman and L. Hu, *Nat. Mater.*, 2016, **16**, 572–579.
- 5 Y. Li, J.-T. Han, C.-A. Wang, H. Xie and J. B. Goodenough, *J. Mater. Chem.*, 2012, **22**, 15357.
- 6 S. Yu, R. D. Schmidt, R. Garcia-Mendez, E. Herbert, N. J. Dudney, J. B. Wolfenstine, J. Sakamoto and D. J. Siegel, *Chem. Mater.*, 2015, **28**, 197–206.
- 7 D. Wang, Q. Sun, J. Luo, J. Liang, Y. Sun, R. Li, K. Adair, L. Zhang, R. Yang, S. Lu, H. Huang and X. Sun, *ACS Appl. Mater. Interfaces*, 2019, **11**, 4954–4961.
- 8 K. H. Noriaki Kamaya, Y. Yamakawa, M. Hirayama, R. Kanno, M. Yonemura, T. Kamiyama, Y. Kato, S. Hama, K. Kawamoto and A. Mitsui, *Nat. Mater.*, 2011, **10**, 682–686.
- 9 H.-J. Deiseroth, S.-T. Kong, H. Eckert, J. Vannahme, C. Reiner, T. Zaiß and M. Schlosser, *Angew. Chem., Int. Ed.*, 2008, **47**, 755–758.
- 10 A. Sakuda, A. Hayashi and M. Tatsumisago, *Sci. Rep.*, 2013, **3**, 2611.
- 11 Y. Zhu, X. He and Y. Mo, *ACS Appl. Mater. Interfaces*, 2015, **7**, 23685–23693.
- 12 Y. Zhu, X. He and Y. Mo, *J. Mater. Chem. A*, 2016, **4**, 3253–3266.
- 13 X. Li, J. Liang, J. Luo, M. Norouzi Banis, C. Wang, W. Li, S. Deng, C. Yu, F. Zhao, Y. Hu, T.-K. Sham, L. Zhang, S. Zhao, S. Lu, H. Huang, R. Li, K. R. Adair and X. Sun, *Energy Environ. Sci.*, 2019, **12**, 2665–2671.
- 14 X. Li, J. Liang, N. Chen, J. Luo, K. R. Adair, C. Wang, M. N. Banis, T. K. Sham, L. Zhang, S. Zhao, S. Lu, H. Huang, R. Li and X. Sun, *Angew. Chem., Int. Ed.*, 2019, **58**, 16427–16432.
- 15 T. Asano, A. Sakai, S. Ouchi, M. Sakaida, A. Miyazaki and S. Hasegawa, *Adv. Mater.*, 2018, **30**, 1803075.
- 16 S. Wang, Q. Bai, A. M. Nolan, Y. Liu, S. Gong, Q. Sun and Y. Mo, *Angew. Chem., Int. Ed.*, 2019, **58**, 8039–8043.
- 17 C. Yu, Y. Li, K. R. Adair, W. Li, K. Goubitz, Y. Zhao, M. J. Willans, M. A. Thijss, C. Wang, F. Zhao, Q. Sun, S. Deng, J. Liang, X. Li, R. Li, T.-K. Sham, H. Huang, S. Lu, S. Zhao, L. Zhang, L. van Eijck, Y. Huang and X. Sun, *Nano Energy*, 2020, **77**, 105097.
- 18 L. Zhou, C. Y. Kwok, A. Shyamsunder, Q. Zhang, X. Wu and L. F. Nazar, *Energy Environ. Sci.*, 2020, **13**, 2056–2063.
- 19 J. Liang, X. Li, S. Wang, K. R. Adair, W. Li, Y. Zhao, C. Wang, Y. Hu, L. Zhang, S. Zhao, S. Lu, H. Huang, R. Li, Y. Mo and X. Sun, *J. Am. Chem. Soc.*, 2020, **142**, 7012–7022.
- 20 K.-H. Park, K. Kaup, A. Assoud, Q. Zhang, X. Wu and L. F. Nazar, *ACS Energy Lett.*, 2020, **5**, 533–539.
- 21 Y. Yu, H. Xu, Z. Wang and G. Shao, *Batteries Supercaps*, 2021, **4**, 1096–1107.
- 22 N. Nitta, F. Wu, J. T. Lee and G. Yushin, *Mater. Today*, 2015, **18**, 252–264.
- 23 X. Li, J. Liang, X. Yang, K. R. Adair, C. Wang, F. Zhao and X. Sun, *Energy Environ. Sci.*, 2020, **13**, 1429–1461.
- 24 Y. Huang, Y. Yu, H. Xu, X. Zhang, Z. Wang and G. Shao, *J. Mater. Chem. A*, 2021, **9**, 14969–14976.
- 25 H. Xu, Y. Yu, Z. Wang and G. Shao, *Energy Environ. Mater.*, 2019, **2**, 234–250.
- 26 H. Xu, W. Xiao, Z. Wang, J. Hu and G. Shao, *J. Energy Chem.*, 2021, **59**, 229–241.
- 27 J. H. G. Kresse, *Phys. Rev. B: Condens. Matter Mater. Phys.*, 1993, **47**, 558–561.
- 28 J. H. G. Kresse, *Phys. Rev. B: Condens. Matter Mater. Phys.*, 1994, **49**, 14251–14269.
- 29 D. J. G. Kresse, *Phys. Rev. B: Condens. Matter Mater. Phys.*, 1999, **59**, 1758–1775.
- 30 P. E. Blöchl, *Phys. Rev. B: Condens. Matter Mater. Phys.*, 1994, **50**, 17953–17979.
- 31 J. H. G. Kresse, *Phys. Rev. B: Condens. Matter Mater. Phys.*, 1993, **48**, 13115–13118.
- 32 J. P. Perdew, K. Burke and M. Ernzerhof, *Phys. Rev. Lett.*, 1996, **77**, 3865–3868.
- 33 G. Shao, *J. Phys. Chem. C*, 2009, **113**, 6800–6808.
- 34 G. Shao, *J. Phys. Chem. C*, 2008, **112**, 18677–18685.
- 35 X. Han, K. Song, L. Lu, Q. Deng, X. Xia and G. Shao, *J. Mater. Chem. C*, 2013, **1**, 3736–3746.
- 36 X. Han and G. Shao, *J. Mater. Chem. C*, 2015, **3**, 530–537.

- 37 Z. Wang, M. Deng, X. Xia, Y. Gao and G. Shao, *Energy Environ. Mater.*, 2018, **1**, 174–178.
- 38 Z. Xiao and Y. Yan, *Adv. Energy Mater.*, 2017, **7**, 1701136.
- 39 C. W. Glass, A. R. Oganov and N. Hansen, *Comput. Phys. Commun.*, 2006, **175**, 713–720.
- 40 A. R. Oganov and C. W. Glass, *J. Chem. Phys.*, 2006, **124**, 244704.
- 41 K. Parlinski, Z. Q. Li and Y. Kawazoe, *Phys. Rev. Lett.*, 1997, **78**, 4063–4066.
- 42 A. Togo, F. Oba and I. Tanaka, *Phys. Rev. B: Condens. Matter Mater. Phys.*, 2008, **78**, 134106.
- 43 M. H. Braga, J. A. Ferreira, V. Stockhausen, J. E. Oliveira and A. El-Azab, *J. Mater. Chem. A*, 2014, **2**, 5470–5480.
- 44 S. P. Ong, Y. Mo, W. D. Richards, L. Miara, H. S. Lee and G. Ceder, *Energy Environ. Sci.*, 2013, **6**, 148–156.
- 45 W. D. Richards, T. Tsujimura, L. J. Miara, Y. Wang, J. C. Kim, S. P. Ong, I. Uechi, N. Suzuki and G. Ceder, *Nat. Commun.*, 2016, **7**, 11009.
- 46 Z. Wang, H. Xu, M. Xuan and G. Shao, *J. Mater. Chem. A*, 2018, **6**, 73–83.
- 47 M. V. Agnihotri, S. H. Chen, C. Beck and S. J. Singer, *J. Phys. Chem. B*, 2014, **118**, 8170–8178.
- 48 M. Xuan, W. Xiao, H. Xu, Y. Shen, Z. Li, S. Zhang, Z. Wang and G. Shao, *J. Mater. Chem. A*, 2018, **6**, 19231–19240.
- 49 Z. Deng, Z. Zhu, I.-H. Chu and S. P. Ong, *Chem. Mater.*, 2017, **29**, 281–288.
- 50 Y. Zhang, Y. Zhao and C. Chen, *Phys. Rev. B: Condens. Matter Mater. Phys.*, 2013, **87**, 134303.
- 51 Z. Wang and G. Shao, *J. Mater. Chem. A*, 2017, **5**, 21846–21857.
- 52 G. L. W. Hart and R. W. Forcade, *Phys. Rev. B: Condens. Matter Mater. Phys.*, 2008, **77**, 224115.
- 53 A. V. D. Walle and G. Ceder, *J. Phase Equilib.*, 2002, **23**, 348–359.
- 54 L. Latie, G. Villeneuve, C. Cros and P. Hagenmuller, *Phys. Status Solidi B*, 1985, **128**, 475–482.
- 55 L. Hanebali, T. Machej, C. Cros and P. Hagenmuller, *Mater. Res. Bull.*, 1981, **16**, 887–901.
- 56 R. Kanno, Y. Takeda, A. Takahashi, O. Yamamoto, R. Suyama and M. Koizumi, *J. Solid State Chem.*, 1987, **71**, 189–195.
- 57 M. Partik, C. Wickel, H. Lutz and T. Roisnel, *J. Solid State Chem.*, 1996, **124**, 292–299.
- 58 H. C. Gupta, J. Zwinscher and H. D. Lutz, *J. Phys. Chem. Solids*, 1997, **58**, 173–175.
- 59 M. Schneider, P. Kuske and H. D. Lutz, *Z. Naturforsch., B: J. Chem. Sci.*, 1993, **48**, 1–6.
- 60 R. Kanno, Y. Takeda and O. Yamamoto, *Solid State Ionics*, 1988, **28**, 1276–1281.
- 61 R. Kanno, Y. Takeda and O. Yamamoto, *Mater. Res. Bull.*, 1981, **16**, 999–1005.
- 62 R. Kanno, Y. Takeda, A. Takahashi, O. Yamamoto, R. Suyama and S. Kume, *J. Solid State Chem.*, 1988, **72**, 363–375.
- 63 Z. Deng, Z. Wang, I.-H. Chu, J. Luo and S. P. Ong, *J. Electrochem. Soc.*, 2015, **163**, A67–A74.
- 64 K. Wakamura, *Phys. Rev. B: Condens. Matter Mater. Phys.*, 1997, **56**, 11593–11599.
- 65 J. C. Bachman, S. Muy, A. Grimaud, H.-H. Chang, N. Pour, S. F. Lux, O. Paschos, F. Maglia, S. Lupart, P. Lamp, L. Giordano and Y. Shao-Horn, *Chem. Rev.*, 2015, **116**, 140–162.
- 66 H. Xu, G. Cao, Y. Shen, Y. Yu, J. Hu, Z. Wang and G. Shao, *Energy Environ. Mater.*, 2021, DOI: 10.1002/eem2.12282.
- 67 Y. Yu, Z. Wang and G. Shao, *J. Mater. Chem. A*, 2018, **6**, 19843–19852.
- 68 Y. Yu, Z. Wang and G. Shao, *J. Mater. Chem. A*, 2019, **7**, 21985–21996.
- 69 Y. Yu, Z. Wang and G. Shao, *J. Mater. Chem. A*, 2019, **7**, 10483–10493.
- 70 G. Shao, *J. Appl. Phys.*, 2000, **88**, 4443–4445.
- 71 G. Shao and P. Tsakiroopoulos, *Philos. Mag. A*, 2000, **80**, 693–710.
- 72 M. H. Braga, A. J. Murchison, J. A. Ferreira, P. Singh and J. B. Goodenough, *Energy Environ. Sci.*, 2016, **9**, 948–954.
- 73 B. Poinard, S. A. E. Lam, K. G. Neoh and J. C. Y. Kah, *J. Controlled Release*, 2019, **300**, 161–173.
- 74 H. Xu, Y. Yu, Z. Wang and G. Shao, *J. Mater. Chem. A*, 2019, **7**, 5239–5247.